Phase Behavior and Dissociation Kinetics of Lamins in a Polymer Model of Progeria

Hadiya Abdul Hameed,[1] Jaroslaw Paturej,[2] and Aykut Erbas[1,2,*]

[1] *UNAM - National Nanotechnology Research Center and Institute of Materials Science and Nanotechnology, Bilkent University, Ankara 06800, Turkiye*

[2] *Institute of Physics, University of Silesia at Katowice, Chorzów, 41-500, Poland*

(Dated: November 8, 2024)

One of the key structural proteins in the eukaryotic cell nucleus is lamin. Lamins can assemble into a quasi-two-dimensional protein meshwork at the nuclear periphery, referred to as the nuclear lamina, which provides rigidity and shape to the nucleus. Mutations in lamin proteins that affect the structure of the nuclear lamina underlie laminopathic diseases, including Hutchinson–Gilford Progeria Syndrome (HGPS). Experiments have shown that, compared to healthy cells, lamin supramolecular structures (e.g., fibers) assemble into a thicker lamina structure in HGPS, where lamins form highly stable nematic microdomains at the nuclear periphery, reminiscent of liquid crystals. This significantly alters the morphological and mechanical properties of the nucleus. In this study, we investigate the aggregation of lamin fibrous structures and their dissociation kinetics from the lamina by modeling them as coarse-grained, rod-like polymer chains confined in a rigid spherical shell. Our model recapitulates the formation of multidirectional nematic domains at the nuclear surface and the reduced lamin dissociation observed in HGPS nuclei by adjusting lamin concentration and lamin-lamin (specifically head-tail) and lamin-nuclear shell association strengths. Particularly, nematic phase formation requires relatively strong lamin-shell affinity under any non-vanishing inter-lamin attraction. Conversely, the dissociation kinetics of lamin rods from the polymer layer at the periphery (lamina) and the thickness of this layer are primarily controlled by head-tail association strength in the model. Our findings can provide molecular-scale insights into the physical mechanisms of lamina assembly, demonstrating how an interplay of altered molecular interactions and lamin concentration can lead to an abnormal lamina in laminopathic diseases.

Keywords: laminopathies, nucleus, progeria, coarse-grained simulations, rod-like polymers

I. INTRODUCTION

The nuclear lamina is a quasi-2-dimensional meshwork structure mainly composed of lamin proteins that are type V intermediate filaments [1–4]. The lamina is located at the nuclear periphery, underneath the inner nuclear membrane (INM)—the phospholipid bilayer of the nuclear envelope that faces the nucleoplasm—and maintains the shape and structural integrity of eukaryotic cell nuclei [5–10]. The nuclear lamina is a highly dynamic meshwork, disassembling during the nuclear envelope breakdown stage of cell division into its molecular components and re-assembling around the replicated decondensing chromosomes [11, 12]. This intricate process requires constituting lamin proteins to self-organize repeatedly and accurately at the nuclear periphery without interfering with the functional and mechanical properties of the nucleus.

The mammalian lamina comprises two main types of lamin proteins: A/C and B-type [2, 8]. Both lamin types share common structural features: a short N-terminal head domain, an α-helical central rod domain, and a globular tail domain [13–15]. The first level of structural assembly of lamin proteins is the formation of a dimer. This occurs when the central rod domains of two lamins coil in a parallel fashion [2, 14–16]. Dimers can further associate with one another to form longer and thicker protofilaments or other higher-order fibrous structures [14, 15, 17] (see Supplementary Material Fig. S1). Lamin fibers of various sizes and thicknesses sterically interact, either directly or indirectly, with each other and the INM [15, 18]. These reversible interactions allow lamin supramolecular structures to localize near the nuclear periphery, around the chromosomes, and form the nuclear lamina meshwork [13, 19, 20]. Both *in vitro* and *in vivo* studies suggest that the lamina is a relatively isotropic network of lamin fibers in healthy cells, exhibiting polymer-network characteristics [21, 22] and node distributions [17, 22, 23]. Regardless, in most healthy cells, lamins are homogeneously distributed across the nuclear boundary resulting in a visually uniform lamina thickness [5, 22].

The molecular structure of the lamina is altered in a class of diseases collectively known as laminopathies. One such disease is Hutchinson–Gilford Progeria Syndrome (HGPS), or briefly progeria, a rare genetic disease that causes the onset of premature aging [6, 8, 24–29]. The main cause of HGPS is a single-point mutation in the *LMNA* gene that encodes human lamin A [30–32]. This mutation produces a truncated form of lamin A, referred to as progerin, which lacks 50 amino acids at the tail domain. Progerin remains permanently farnesylated following post-translational modifications, unlike mature lamin A [24, 25, 27, 33–35]. Since farnesylation

* aykut.erbas@unam.bilkent.edu.tr

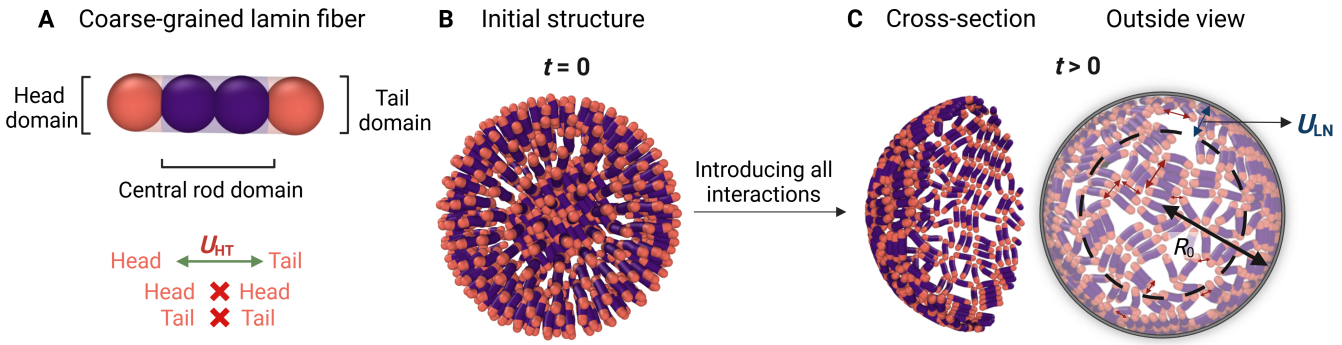

FIG. 1. The schematics of the MD simulation model and simulation steps. (A) Coarse-grained lamin chain with head, tail, and central domain. The head and tail domains are allowed to associate with one another and are marked with the same color for simplification. (B-C) Illustration of the MD simulation steps. (B) The initial structure is minimized for 10^4 MD time steps. (C) After minimization, the head-tail association potential, U_{HT}, and lamin-shell interaction, U_{LN}, are switched on and the simulation runs for another 10^5 MD time steps.

can enhance hydrophobic interactions, it can promote a stronger binding tendency of mutated lamin A (i.e., progerin) towards the INM or other hydroponic components of the lamina. These alterations, in turn, lead to anomalies in the morphology and mechanical properties of cell nuclei in progeria [20, 36, 37], significantly decreasing cell viability.

In the progression of HGPS, as the nuclear concentration of mutant lamin A increases, the nucleus becomes more mechanically rigid and morphologically distorted upon the accumulation of lamins at the nuclear lamina [34, 38–43]. Polarization light microscopy experiments further elucidated that lamins form orientally ordered, uncorrelated nematic domains in the nuclear lamina of HGPS nuclei, each large enough to display birefringence [7]. On the contrary, no birefringent pattern was observed at the lamina of healthy nuclei, suggesting a presence of randomly oriented lamin filaments [7, 41, 44]. Notably, studies also suggest that both wild-type lamin A (*wt*-lamin A) and progerin can form paracrystalline phases *in vitro* [15, 36], a property encountered in the solutions of rod-like molecules with high bending rigidity (e.g., liquid crystals) [45–47]. More specifically, when confined by convex spherical surfaces, short (i.e., compared to the dimensions of the confining shell) polymer chains with high bending rigidity (e.g., rod-like) exhibit nematic phases in computational simulations [48–51]. This, combined with the available experimental data, indicates that the formation of nematic phase domains observed in nuclei of most laminopathic cells could be a consequence of irregular biomolecular interactions promoting increased localization of mutant lamins to the nuclear periphery.

Experiments further suggest that the dissociation properties of lamin proteins are altered in HGPS cells. Photobleaching experiments have shown that nucleoplasmic and peripheral lamins exchange with one another in healthy cells [7], further confirming that lamins can interact transiently with the lamina [52, 53]. In contrast to a healthy lamina, in progeria, mutated lamin A, progerin, is irreversibly associated with the INM, exhibiting much weaker exchange kinetics with its solution counterparts compared to *wt*-lamin A [7, 26]. This points to a potential correlation between lamina's structural and kinetic properties in disease.

Overall, experimental evidence suggests that lamin proteins' assembly and organization in the nuclear lamina are affected by lamin concentration and lamin affinity toward one another or the INM. Nevertheless, these factors' relative biophysical roles in determining the nuclear lamina's micro-scale properties, particularly in disease phenotypes, are relatively poorly understood. While a limited number of computational studies provide insights into the formation of misshapen nuclei, such as those observed in HGPS [9], exploring physical interactions and stoichiometric conditions that can lead to the multi-directional nematic domains and thicker lamina in laminopathies can help decipher the universal principles of the disease progression.

While the nuclear lamina is a highly complex biomolecular structure, the formation of this protein meshwork requires i) localization of lamin proteins to the periphery, ii) a relatively stable inter-lamin association that can maintain the shape of the nucleus under mechanical forces, and iii) a sufficiently large lamin concentration to coat the inner nuclear surface. To study these primary mechanisms involved in lamin assembly, we devise a simple molecular dynamics (MD) model for lamin fibers and consider them as a monodisperse solution of rod-like polymer chains confined in a spherical volume representing the nuclear void (Fig. 1). Focusing particularly on the effect of lamin concentration, head-tail association strength between lamin fibers, and lamin-nuclear shell interactions, we emulate the formation of nematic phase domains and lamina thickening reported in HGPS while correlating slow lamin dissociation and lamina thicken-

ing observed in diseased nuclei. Our study suggests that the concentration of lamin proteins alone cannot dictate their exchange kinetics or nuclear lamina thickening. Instead, there also needs to be a compromise between the strength of the head-tail lamin association and the interaction of lamins with the INM.

II. METHOD

A. Molecular model of nuclear lamins

In the nucleoplasm, individual lamin proteins are not solvated, but rather exist in their dimer form [2, 8], On the contrary, lamins typically aggregate near the nuclear boundary as more complex fibrous structures with large aspect ratios [17, 43]. Thus, in our study, each lamin fiber is approximated as a Kremer-Grest (KG) rod-like, bead-spring chain in implicit solvent (Fig. 1*A*) [54]. These semi-flexible chains can model relatively thick lamin complexes (e.g., short protofilaments).

Given that HGPS and other laminopathies are predominantly associated with mutations in A-type lamins, rather than B-type, we focus on modeling a single type of lamin [30]. A-type lamins also play a key role in regulating the nuclear shape and stiffness [28, 31, 55]. In the KG model, the bead size is set to $b = 1\sigma$, which defines the unit length scale in our simulations. The beads representing the head, tail, and central rod domains are all the same size, with each lamin fiber consisting of $n = 4$ beads unless otherwise specified. Using longer chains, i.e., $n = 8$ or $n = 16$, does not affect our results qualitatively (see Supplementary Material Fig. S2-S7). The terminal beads correspond to head and tail domains (Fig. 1*A*). The lamin fibers are confined within a rigid spherical boundary of radius, R_0, to mimic the steric effect of the nuclear envelope (Fig. 1*C*). The spherical confinement has a radius, $R_0 = 17\sigma$, unless specified otherwise (Fig. 1) (see Supplementary Material).

Assuming a nuclear diameter of $d \approx 10$ μm, and an approximate lamin fiber length of $l \approx 400$ nm [5, 55, 56], the number of lamins required to cover the surface of the nucleus is estimated to be $N \approx (10\ \mu m/4 \times 10^2$ nm$)^2 \approx 10^3$. Accordingly, the number of semi-flexible rods in our rigid, spherical nucleus model varies between $N = 500$ and $N = 2000$. This range corresponds to lamin concentrations above and below the overlap concentration, c^*, in the bulk. The overlap concentration, c^*, represents the point at which the lamin rods in our simulations transition from a dilute to a semi-dilute regime. This concentration marks where individual lamin fibers begin to overlap and interact with one another.

$$c^* = \frac{n}{v} \tag{1}$$

where $v \approx l^3 \approx n^3\sigma^3$ is the pervaded volume of a single lamin rod. The overlap concentration for 4-bead lamin rods, $n = 4$, is $c^* \approx 0.1\sigma^{-3}$. The concentration values used in the simulations are shown in Table I.

TABLE I. Conversion of number of chains (N) to concentration (c in σ^{-3} and c in terms of c^*)

N	$c(\sigma^{-3})$	c/c^*
500	0.097	0.8
750	0.15	1.2
1000	0.19	1.6
1250	0.24	2.0
1500	0.30	2.4
2000	0.39	3.3

B. Simulation setup

In simulations, lamin rods are initially placed randomly within the spherical confinement (Fig. 1*B*). We verified that the initial configuration does not affect simulation results (see Supplementary Material Fig. S8). We minimize the energy of the initial lamin configuration for 10^4 MD time steps (Fig. 1*B*) using an integration time step of $\Delta t = 0.001\tau$, where τ is the unit of time in the simulations. Following the minimization, each system undergoes an additional 10^5 MD time steps with $\Delta t = 0.005\tau$. During the production phase of the simulations, attractive lamin-shell and lamin-lamin interactions are introduced to the relaxed configuration to replicate healthy and diseased nuclear lamina phenotypes. The spherical confinement exerts an attractive potential, U_{LN}, mimicking the interaction between the lamin fibers and the nuclear periphery (e.g., with the INM) (Fig. 1*C*). Since lamin proteins can assemble via head-tail interactions [2, 15], the head domain of each lamin interacts exclusively with the tail domain of other lamins through a head-tail association potential, U_{HT} (Fig. 1*A*).

The non-bonded, steric interactions between beads and with the confining surface are modeled using the Lennard-Jones (LJ) potential:

$$V(r_{ij}) = 4\epsilon\left[\left(\frac{\sigma}{r_{ij}}\right)^{12} - \left(\frac{\sigma}{r_{ij}}\right)^{6}\right] \quad \text{for} \quad r \le r_c, \tag{2}$$

where ϵ represents the energy unit, r_{ij} is the distance between two beads, and r_c is the cut-off distance beyond which the LJ potential becomes negligible. For attractive interactions, such as head-tail and lamin-shell interactions, r_c is set to 2.5σ. For all other interactions, the cut-off radius is set to $r_c = 2^{1/6}\sigma$ to ensure steric repulsion. The default value of the interaction strength in Eq. 2 is $\epsilon = 1k_{\mathrm{B}}T$, where k_{B} is the Boltzmann constant and T is the reduced absolute temperature, i.e., unity in our simulations. The attraction between the head and tail beads of lamin chains, U_{HT}, as well as between lamins and the confining, structureless, surface, U_{LN}, is adjusted by increasing ϵ in Eq. 2.

All bonded interactions between adjacent beads in each lamin fiber are described using a Finitely Extensible Non-

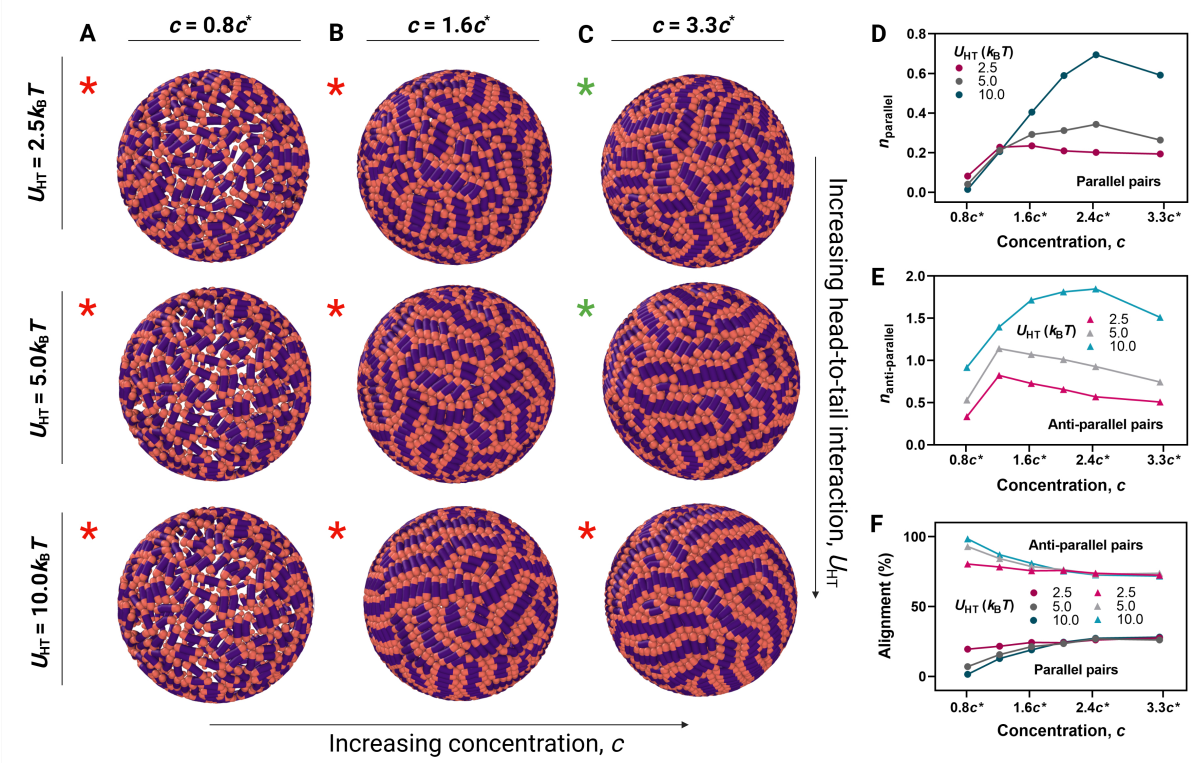

FIG. 2. Isotropic and nematic phase formation of lamin chains at the nuclear lamina surface and exchange at the interior. Red asterisks (*) represent cases where lamins are restricted at the nuclear periphery, while green asterisks (*) represent the kinetic exchange regime described in Eq. 5. (A–C) Representative snapshots of the rigid, model nucleus at various head-to-tail association potentials, U_{HT}, with lamin concentrations, $c = (A)\ 0.8c^*$, $(B)\ 1.6c^*$, and $(C)\ 3.3c^*$ at a fixed lamin-shell interaction strength, $U_{\mathrm{LN}} = 10.0k_{\mathrm{B}}T$. Normalized number of ($D$) parallel lamin pairs, n_{parallel}, and (E) anti-parallel pairs, $n_{\mathrm{anti-parallel}}$, with respect to concentration at various head-tail association potentials, U_{HT}. (F) Percentage alignment of lamin rod pairs (anti-parallel pairs at the top, parallel pairs at the bottom) as a function of concentration, c, at various head-tail association potentials, U_{HT}.

linear Elastic (FENE) potential:

$$V_{\mathrm{Bond}}(r_{ij}) = -0.5kr_{ij}^2 \ln\left[1 - \left(\frac{r_{ij}}{r_0}\right)^2\right], \qquad (3)$$

where the bond energy is set to $k = 30.0k_{\mathrm{B}}\,T/\sigma^2$ and the maximum bond distance is set to $r_0 = 1.5\sigma$.

The bending fluctuations of lamin chains are constrained by a harmonic angle potential in the form of

$$V_{\mathrm{Bend}}(\Theta) = k_{\Theta}(\Theta - \Theta_0)^2, \qquad (4)$$

where the bending energy is set to $k_{\Theta} = 10.0k_{\mathrm{B}}T/rad^2$, and the reference angle is $\Theta_0 = \pi$. These parameters result in a persistence length higher than the length of each lamin chain, $l_p > l$, ensuring that they behave predominantly as rod-like structures in the simulations (see Supplementary Material Fig. S9). All energies are defined in thermal energy units, $k_{\mathrm{B}}T$ ($\approx 0.6\ kcal/mol$).

All simulations were carried out in the LAMMPS MD simulations package [57]. Various Python libraries are used for data analysis [58]. VMD and OVITO were used for structural visualization [59, 60].

C. Kinetic calculations

To quantify the kinetic behavior of lamin rods, we monitor the dissociation of peripherally localized chains across various binding affinities (U_{HT} and U_{LN}) and lamin concentrations, c. Specifically, we measure the decay of the population of peripherally *bound* lamin fibers, while those freely diffusing in the nucleoplasm are considered *unbound*. As the simulation progresses, the initially bound lamins, n_0, dissociate and exchange with those in the nucleoplasm. The number of remaining bound lamins, $n(t)$, is calculated as a function of the time, t (see Supplementary Material Fig. S10). A lamin is considered dissociated and tagged as unbound if it moves beyond a defined cut-off radius, R_{C}, from the nuclear periphery. If a dissociated lamin protein rebinds to the spherical confinement, it is not counted again as part of the surviving lamins, $n(t)$. The dissociation cut-off distance is set to the size of a single chain, $R_0 < R_{\mathrm{C}} \leq 4\sigma$ [61, 62] (see Supplementary Material Fig. S11), and varies with the thickness, δ, of the nuclear lamina, which depends on lamin concentration. For the analysis, only the latter half of each simulation is considered, excluding the ini-

tial equilibration phase of lamin organization. A single-exponential fit is applied to model lamin dissociation and determine off-rates:

$$\frac{n(t)}{n_0} = a + b\exp(-k_{\rm off}t), \tag{5}$$

where $k_{\rm off}$ is the off-rate with the units of inverse simulation time, while a and b are fitting parameters. The fit is specifically applied when the bound lamin fraction satisfies $n(t)/n_0 \leq 0.5$, ensuring that it captures the later stages of dissociation, where the exponential decay behavior is most prominent.

III. RESULTS

In our simulations, most lamin rods first localize near the spherical boundary at $t > 0$, forming a layer of adsorbed chains (Fig. 1C). We will refer to this layer as "lamina". While we observe aggregates at the center in some cases (see Supplementary material Fig. S12), especially for longer chains, these structures vanish as the simulation time is extended. Once some or all of the chains are localized to the periphery, this is followed by either lamin dissociation or stable accumulation of chains to the spherical boundary depending on the lamin concentration, c, head-to-tail association strength, $U_{\rm HT}$, and the interaction of lamin rods with the interior surface of our spherical confinement, $U_{\rm LN}$.

A. Nematic phase formation of model lamin chains on the spherical surface occurs beyond the threshold concentration, c^*

To explore molecular conditions affecting the morphology and organization of lamin proteins in the nuclear lamina assembly, we first analyze the effect of lamin chain concentration in a model nucleus in our simulations. We scan the concentrations above and below the threshold concentration, c^*, (Eq. 1), where lamin chains can be at steric contact in the bulk (Table I). Since we compare two interactions in our model, $U_{\rm LN}$ and $U_{\rm HT}$, we investigate their relative contribution to the nuclear lamina assembly process systematically. To do so, we first choose a high lamin-shell interaction strength, $U_{\rm LN} = 10.0k_{\rm B}T$, while changing the head-tail association potential. This ensures the localization of lamin chains near the boundary of the spherical confinement. The effect of $U_{\rm LN}$ will be discussed in detail in the upcoming chapters. For the head-tail attraction strength, three values, $U_{\rm HT} = 2.5$, 5.0, and $10.0k_{\rm B}T$, are chosen. These values are weaker than and equal to the lamin-shell attraction, but higher than the thermal energy scale, i.e., $\approx k_{\rm B}T$.

Fig. 2 shows representative simulation snapshots taken from the final stage of different simulations at various concentrations. These simulations reveal that concentration directly affects the morphology of lamin phases localized at the inner surface of the model nucleus, particularly when lamin chains have a strong affinity towards the confining boundary, $U_{\rm LN} = 10.0k_{\rm B}T$. At low concentrations (i.e., $c \leq c^*$), lamin chains are arranged with no specific directional order regardless of the head-tail attraction strength (Fig. 2A, top to bottom). Notably, increasing the head-tail association strength does not affect their isotropic orientation. In fact, at such concentrations, despite the absence of any rod-rod attraction other than that defined between the head and tail domains, chains organize in groups, leaving small chain-free regions on the surface (Fig. 2A). At intermediate to high concentrations, $c > c^*$, local nematic phases appear on the surface and cover the entire inner surface of the spherical confinement (Fig. 2B, C). These phases are different than global phases of long semi-flexible chains reported earlier [49–51] and are visually non-percolating, irrespective of the head-tail association strength, $U_{\rm HT}$. These lamin phases are consistent with the nematically ordered domains reported for lamin organization on lamina *in vivo* and *in vitro* [6, 7, 36].

To understand the nematic phase formation on the surface quantitatively, we attempt to use methodologies that were used to study the nematic liquid crystalline phases of semi-flexible polymers [48, 63]. Accordingly, the diagonalization of the configurational tensor for all the chains provides information if all chains form a global nematic order in bulk or on surface [48–51]. Nevertheless, in our system, where the surface is covered by nematic domains, each pointing in a random direction as shown in Fig. 2, such a method does not distinguish between nematically ordered and isotropic domains. Thus, we rather choose to calculate a spin-spin-like order parameter, such that if a chain aligns parallel or anti-parallel to its nearest neighbor, the order parameter is either $S = \pm 1$ or; otherwise, it is 0. Averaging over pairs obeying the nearest neighbor criterium ($r_{\rm nm} < 1.5\sigma$) on the surface demonstrates the dependence of lamin ordering on the concentration and head-tail affinity (Fig. 2D-F). With weak head-tail association (i.e., $U_{\rm HT} = 2.5k_{\rm B}T$), the sum of the ratios of parallel and anti-parallel pairs are less than half, suggesting more randomly oriented pairs on the surface. Increasing head-tail affinity increases the number of both parallel and anti-parallel pairs (Fig. 2D, E), each of which is parallel to the surface (see Supplementary material Fig. S13). Notably, most chains obey an anti-parallel ordering within domains since the asymmetric head-tail association potentially favors such ordering over the parallel ordering within each domain (Fig. 2E). While both parallel and anti-parallel pairs increase with concentration, this increase becomes non-monotonical at the highest concentration we use here (Fig. 2D, E). As we will discuss further in the next section, increasing layer thickness could affect the ordering of the chains at such concentrations. These analyses suggest that while concentrations significantly above c^* lead to nematic domains, once chains are localized to the surface, the head-tail association strength controls the extent of this domain formation. In fact, at

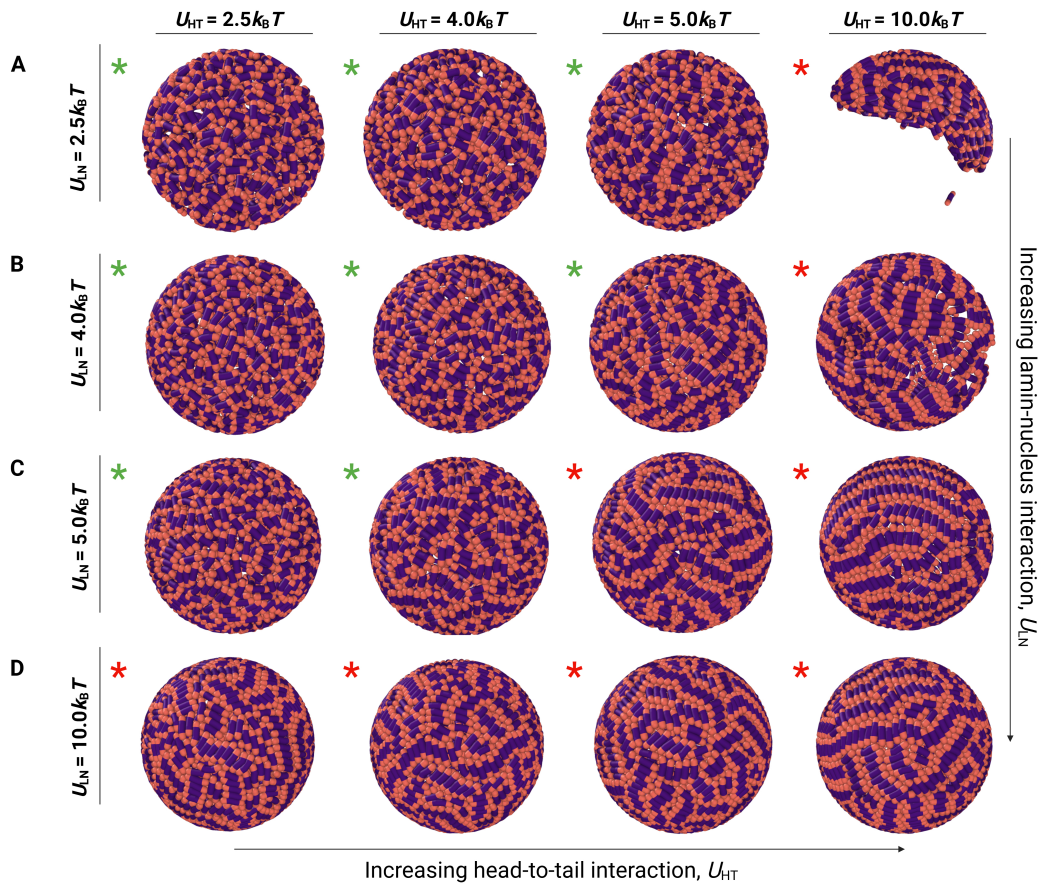

FIG. 3. Representative snapshots demonstrating the interplay of U_{LN} and U_{HT} at fixed concentration, $c = 1.6c^*$. (A-D) Isotropic to nematic phase transition of lamin fibers at $c \approx c^*$. Lamin proteins are randomly organized into isotropic domains at lower lamin-shell association potentials i.e., $U_{\mathrm{LN}} = (A)\ 2.5k_{\mathrm{B}}T$. Head-tail association potential seems to play a partial role in organizing lamin proteins at intermediate $U_{\mathrm{LN}} = (B)\ 4.0$, and $(C)\ 5.0k_{\mathrm{B}}T$. (D) Organized microdomain formation is observed when the lamin-shell attraction is high, i.e., $U_{\mathrm{LN}} = 10.0k_{\mathrm{B}}T$.

$U_{\mathrm{HT}} = 0$, no phases are observed on the surface (see Supplementary material Fig. S14).

Overall, these simulations suggest that the strong localization of lamins on the nuclear surface can exhibit a transition from isotropic to nematic domains with increasing concentration of lamin species.

B. Nematic phase formation on the shell surface is a result of the competition between lamin-lamin and lamin-shell interactions

Having demonstrated that nematic phase formation of lamin chains on the shell surface is weakly dependent on the head-to-tail interaction strength, U_{HT}, when lamin-shell attraction, U_{LN}, is strong enough (i.e., $U_{\mathrm{LN}} \geq U_{\mathrm{HT}}$) (Fig. 2), we next explore whether this trend persists for weaker U_{LN} cases. In this investigation, a concentration slightly above the threshold value (i.e., $c = 1.6c^*$) is chosen to ensure that we observe nematic phases (see Supplementary material Fig. S15 for a higher concentration). In Fig. 3, from left to right, we increase the lamin-lamin (head-tail) attraction, U_{HT}, while lamin-shell attraction, U_{LN}, is increased from top to bottom in separate simulations.

In general, weaker lamin-shell association strength (i.e., $U_{\mathrm{LN}} \ll U_{\mathrm{HT}}$) leads to either isotropic chain organization or complete disruption of the peripheral organization of lamin chains, depending on the strength of head-tail attraction (Fig. 3A, B). For instance, when $U_{\mathrm{LN}} = 2.5k_{\mathrm{B}}T$, no nematic domains emerge until head-tail association potential is high enough (i.e., $U_{\mathrm{HT}} = 10.0k_{\mathrm{B}}T$), where a spherically asymmetric aggregation of chains forms at the boundary of the confinement (Fig. 3A), which becomes more dominant under weaker shell association (see Supplementary material Fig. S16). While lamin chains align in the local domains of nematic order in these aggregates, they also tend to coalesce at the interior of the spherical confinement, resulting in large lamin-free regions at the periphery (right column of Fig. 3A). The intermediate values of lamin-shell attraction strengths tested here, $U_{\mathrm{LN}} = 4.0,\ 5.0k_{\mathrm{B}}T$, are

also sufficient to align the chains parallel to one another (see Supplementary material Fig. S17, S18). However, in these cases, sparse lamin-free regions also emerge, confirming that high lamin-shell association is needed to coat the surface completely (Fig. 3*B*, *C*). As the lamin-shell association strength is increased to $U_{\mathrm{LN}} = 10.0k_{\mathrm{B}}T$, this trend disappears, and lamin chains cover the entire surface symmetrically, irrespective of the strength of head-tail attraction (Fig. 3*D*).

Overall, our simulations suggest that mutations increasing lamin association with INM can be pivotal for the accumulation of lamin chains near the periphery. Nevertheless, such a pattern can be distorted if the lamin-lamin attraction excessively overcomes lamin-shell attraction. In the next sections, we will discuss how these interactions might govern the effective thickness of the lamin (rod) layer and the dissociation kinetics of lamin chains from the layer.

C. Thickness of the lamin layer, δ, increases with increasing ratio of affinities lamin-lamin association and concentration, c

Our analyses in the previous sections demonstrate that lamin chains can coat the inner surface of the spherical confinement (Fig. 2, 3). Nevertheless, in simulations, lamin chains over-saturate the surface, thus leading to thicker, non-uniformly distributed chain aggregates at the periphery under certain conditions (see Supplementary Material Fig. S19). This behavior can be comparable with thicker lamina in disease phenotypes [8, 22, 64].

To quantify the thickness of the lamin chain layer in our simulations, we analyze the radial distributions of the lamin chains in the model spherical nucleus. We calculate the positional fluctuations, dr, of the center-of-mass-adjusted radial distances for each chain over the simulation time. As the simulation proceeds, if the radial coordinate of a lamin chain fluctuates weakly (i.e., less than the unit size of a bead, $dr \leq 0.25$) near the shell boundary, the lamin chain is considered immobile and *bound* (Fig. 4*A*). The time-averaged radial position, R, of this chain contributes to the thickness of the nuclear lamina via the expression

$$\delta = R_0 - \langle R \rangle, \tag{6}$$

where R_0 is the radius of spherical confinement used to simulate the nucleus (Fig. 1*C*), and $\langle R \rangle$ is the average radial position of all lamin chains fulfilling the *bound* condition.

Fig. 4 shows the thickness of the lamin layer, calculated via Eq. 6, as a function of normalized concentration for various ratios of head-tail to lamin-shell affinities, $U_{\mathrm{HT}}/U_{\mathrm{LN}}$. At the lowest concentration we use here (i.e., $c \leq c^*$), the number of lamin chains in the spherical confinement is only enough to form a single layer with a thickness $\delta \approx 1.3\sigma$ if lamin-shell interactions are comparable or stronger than lamin-lamin association strength (Fig. 4*B*, *F*, *G*). If the lamin-shell attraction is strong at low concentration, we observe a chain-free section on the surface (Fig. 3, 4*H*). At intermediate (i.e., $c \approx c^*$) to high (i.e., $c > 2c^*$) concentrations, the thickness becomes dependent on the ratio of the two competing interactions. For $U_{\mathrm{HT}}/U_{\mathrm{LN}} < 1$, the thickness has no dependence on concentration (Fig. 4*B*, *F*). Notably, at such ratios, there are unbound, freely diffusing chains in the bulk (Fig. 4*F*). As the ratio $U_{\mathrm{HT}}/U_{\mathrm{LN}}$ is increased, the effect of concentration becomes more dominant, resulting in the formation of chain multilayers covering the entire surface (Fig. 4*B*, *G*). In fact, if we combine more than 20 data points given in Fig. 4*B* and plot them as a function of $U_{\mathrm{HT}}/U_{\mathrm{LN}}$, the interplay between the concentration and relative affinities becomes more evident (Fig. 4*D*). If the head-tail attraction is considerably stronger than the lamin-shell affinity (i.e., $U_{\mathrm{HT}}/U_{\mathrm{LN}} > 1$), at high concentration levels, the thickness increases up to $\delta \approx 2\sigma$, but the distribution of chains at the periphery is higly non-uniform (Fig. 4*B*, *H*).

To further quantify the partitioning of lamin proteins into *bound* (i.e., those forming the nuclear lamina layer) and *unbound* (i.e., free, nucleoplasmic) phases, we also calculate the radial probability distributions, $p(r)$, by counting the number of lamin chains, $n(r)$, in a thin slice of the shell's volume with width $\Delta r = 1\sigma$:

$$p(r) = \frac{n(r)}{4\pi R_0^2 \Delta r}. \tag{7}$$

The radial probability distribution for various affinity ratios is consistent with the thickness calculations (Fig. 4*C*, *E*). At low lamin-lamin interaction strengths with fixed $U_{\mathrm{LN}} = 10.0k_{\mathrm{B}}T$, specifically $U_{\mathrm{HT}}/U_{\mathrm{LN}} = 0.25$, the nuclear lamins are distributed throughout the confinement, co-existing in both the central and peripheral regions of the volume (Fig. 4*C*, *F*). In contrast, at higher lamin-lamin affinities (i.e., $U_{\mathrm{HT}}/U_{\mathrm{LN}} = 1.0$), lamin chains localize at the periphery, leaving the bulk lamin-free (Fig. 4*C*, *E*, *G*). Notably, larger error bars in $U_{\mathrm{HT}}/U_{\mathrm{LN}} > 1$ case are consistent with the non-uniform chain distribution and the larger thickness of the layer at the periphery. The relatively strong head-tail association strength (i.e., $U_{\mathrm{HT}} \geq U_{\mathrm{LN}}$) indeed can result in completely lamin-free peripheral regions while increasing the thickness to several times the chain size (Fig. 3*A*, 4*H*).

Collectively, these simulations demonstrate that while weak lamin-shell association can localize some lamin proteins at the periphery, the thickening and accumulation at the lamin layer in our simulations is primarily controlled by head-tail association affinity, U_{HT}. This interaction can lead to the phase segregation of various lamin types at the nuclear periphery [9] while contributing to the partial thickening of the nuclear lamina in disease.

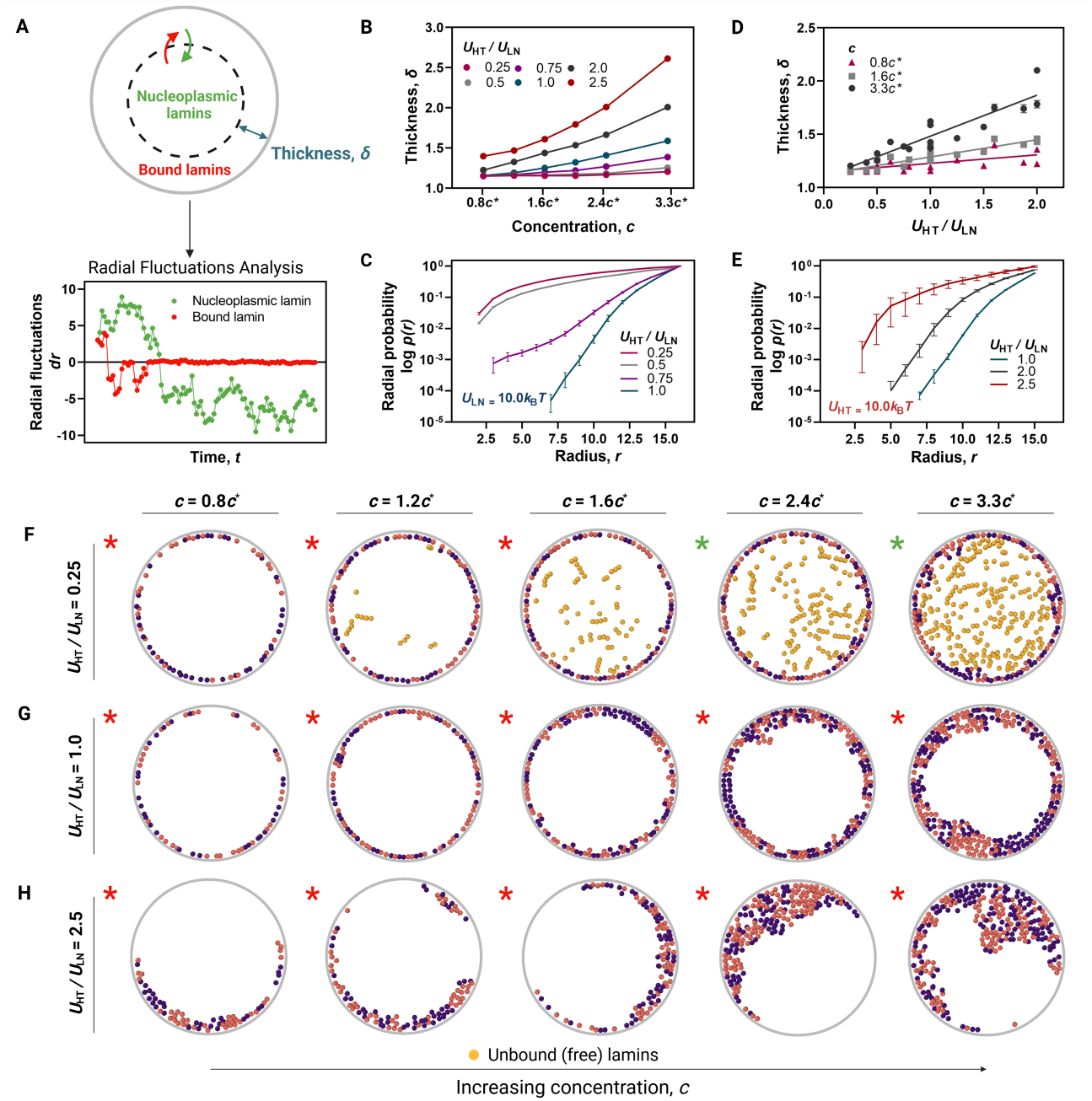

FIG. 4. The effect of U_{HT}, U_{LN}, and concentration, c, on the thickness of the nuclear lamina. (A) Calculation of the thickness, δ, of the nuclear lamina. The graph shows the fluctuation of radial coordinates for a single *bound* and *unbound* lamin. A lamin is considered *bound* to the nuclear periphery if its radial coordinate stops fluctuating significantly over time as the simulation proceeds. (B) Nuclear lamina thickness, δ, vs. concentration, c, at various $U_{\mathrm{HT}}/U_{\mathrm{LN}}$. ($C$) Logarithm of radial probability distribution, $p(r)$, as a function of radial distance, r, at 4 different $U_{\mathrm{HT}}/U_{\mathrm{LN}}$ for $c = 3.3c^*$ and $U_{\mathrm{LN}} = 10.0k_{\mathrm{B}}T$. ($D$) Thickness, δ, vs. ratio of affinities, $U_{\mathrm{HT}}/U_{\mathrm{LN}}$, at 3 concentrations i.e., $c = 0.8c^*$, $1.6c^*$, and $3.3c^*$. (E) Logarithm of radial probability distribution, $p(r)$, as a function of radial distance, r, at 3 different $U_{\mathrm{HT}}/U_{\mathrm{LN}}$ for $c = 3.3c^*$ and $U_{\mathrm{HT}} = 10.0k_{\mathrm{B}}T$. ($F$-$H$) Snapshots of 1σ wide slices from the center of the nucleus at various lamin concentrations for $U_{\mathrm{HT}}/U_{\mathrm{LN}} =$ (F) 0.25, (G) 1.0, and (H) 2.5. Yellow chains represent *unbound* lamin proteins participating in the kinetic exchange.

D. Extent of lamin chain dissociation depends on head-tail association strength, U_{HT}, and concentration, c.

One particular hallmark of HGPS is the suppressed dissociation of mutant lamins from the nuclear lamina [7]. In accordance with those studies, in some of our simulations, lamin chains unbind from and rebind to the periphery (Fig. 4F). In other cases, they are more stably bound to the peripheral aggregates (Fig. 4G, H).

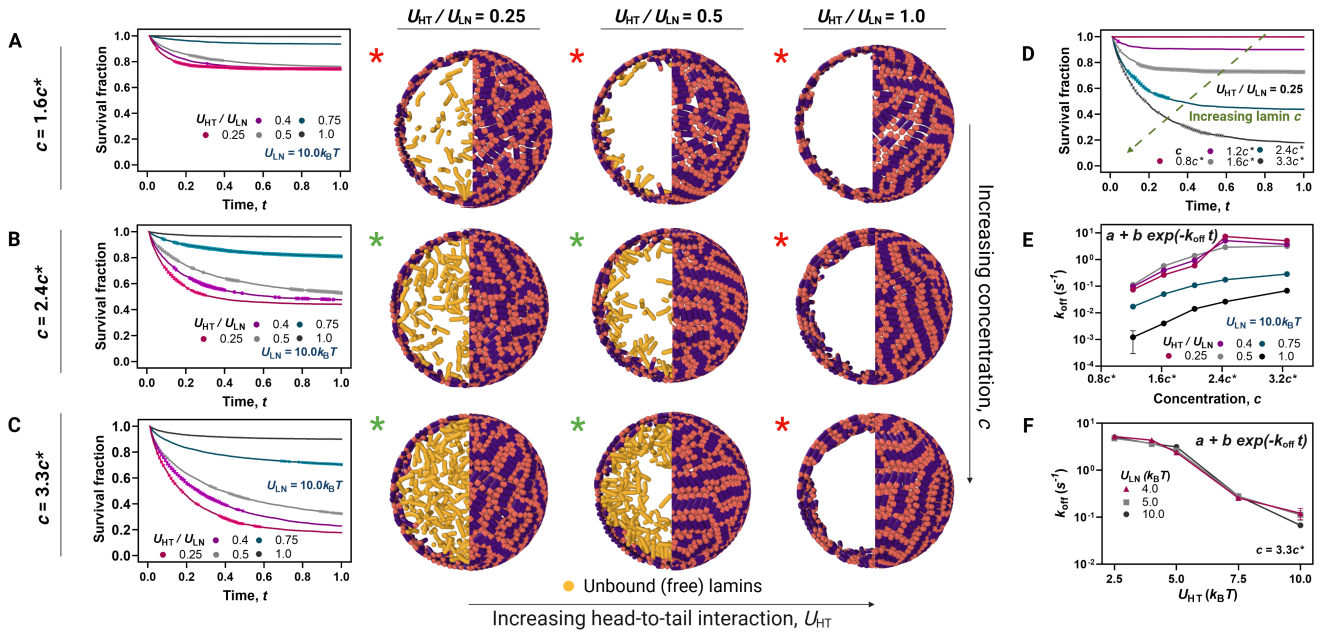

FIG. 5. The dependence of lamin dissociation kinetics on concentration, c, and ratio of head-to-tail association potential to lamin-shell affinity, $U_{\mathrm{HT}}/U_{\mathrm{LN}}$. Graphs on the left represent the behavior of the normalized survival fraction, $n(t)/n_0$, of *bound* nuclear lamins over time, t. The solid curves are the exponential fits (Eq. 5). Snapshots in the middle show 10σ wide slices from the center of the model nucleus. Yellow chains represent *unbound*, free lamin proteins participating in a kinetic exchange. (A-C) Illustrations representing the degree of exchange between nucleoplasmic and shell-bound lamins at three different concentrations: $c = (A)\ 1.6c^*$, $(B)\ 2.4c^*$, and $(C)\ 3.3c^*$ at fixed $U_{\mathrm{LN}} = 10.0k_{\mathrm{B}}T$. ($D$) Time-dependent decay curve for lamin dissociation at various concentrations to extract off-rates, k_{off}, from the fraction of remaining *bound* lamins over time with fixed $U_{\mathrm{HT}}/U_{\mathrm{LN}} = 0.25$. ($E$-$F$) Off-rates extracted from the survival fraction data. (E) Off-rates as a function of lamin concentration for various $U_{\mathrm{HT}}/U_{\mathrm{LN}}$ at fixed $U_{\mathrm{LN}} = 10.0k_{\mathrm{B}}T$. ($F$) Off-rates as a function of head-tail association potential, U_{HT}, for various U_{LN} at a fixed concentration, $c = 3.3c^*$.

To quantify lamin dissociation kinetics thoroughly in our simulations, we calculate the survival fraction of bound lamins as a function of normalized simulation time, t, for various concentration and affinity cases (see Methods Section). For simplicity, we choose a fixed lamin-shell attraction strength, $U_{\mathrm{LN}} = 10.0k_{\mathrm{B}}T$, and vary the head-tail association energy. However, reducing the strength of lamin-shell attraction from $U_{\mathrm{LN}} = 10.0k_{\mathrm{B}}T$ does not change the lamin dissociation patterns discussed below (see Supplementary Material Fig. S19-S22).

In our analyses, we observe that, at a concentration slightly above c^* (i.e., $c = 1.6c^*$), increasing the head-tail association strength leads to almost no decay in the survival fraction curve in the duration of the simulation if head-tail association strength is equal to the lamin-shell association (i.e., $U_{\mathrm{HT}}/U_{\mathrm{LN}} = 1$), indicating stably bound lamin chains (Fig. 5A). Noteworthy, slow lamin dissociation overlaps with chain accumulation at the periphery (i.e., thicker lamin layer in Fig. 4G). Lowering the relative strength of the head-tail affinity (i.e., $U_{\mathrm{HT}}/U_{\mathrm{LN}} < 1$) increases the population of free lamin chains within the spherical shell (Fig. 5A-C, 4F). If the lamin concentration is increased further to $c > 2c^*$, this trend persists, but the lamin dissociation accelerates significantly: more than half of the bound lamins dissociate within the first half of the simulation time at $c = 2.4c^*$ and $3.3c^*$(Fig. 5B, C). A visual inspection distinguishing between bound and free lamins (yellow beads in Fig. 5) indicates that the presence of free chains in bulk enhances the sensitivity of the survival fraction to concentration changes.

We further quantify the effect of concentration by plotting survival fractions at various concentrations, while keeping the ratio of affinities fixed at $U_{\mathrm{HT}}/U_{\mathrm{LN}} = 0.25$ (Fig. 5D). The survival fraction decays more rapidly with increasing concentration, indicating a competition-driven exchange mechanism [47, 61, 65]. Fitting survival fraction data to the exponential function in Eq. 5 leads to the off-rates for lamin chains dissociating from the periphery [66]. Plotting the off-rates as a function of the total chain concentration reveals a clear concentration-dependent trend of the off-rates for a wide range of head-tail affinities (Fig. 5E) (see Supplementary Material Fig. S22, S23).

The general trend is that the off-rates increase monotonically with concentration, eventually approaching a saturation limit at concentrations well above the overlap concentration, $c > 2c^*$ (Fig. 5E). This pattern is consistent with a facilitated dissociation (FD) response, where an increase in the concentration of competing species in solution can lead to higher off-rates (i.e., shorter resi-

dence times) [61, 62, 65, 66] (see Supplementary Material Fig. S1, S2). Accordingly, when there is a high concentration of free nucleoplasmic lamins, they can compete with the *bound* lamins at the nuclear lamina and speed up their dissociation. In that case, the off-rate becomes concentration dependent following, and this dependence can be expressed as [43, 67]:

$$k_{\text{off}} = k_{\text{slow}}^{(0)} + ck_1, \tag{8}$$

where $k_{slow}^{(0)}$ is the off-rate in the absence of competing species, and the product ck_1 represents the off-rate component arising from the partial association-dissociation behavior of nucleoplasmic lamin proteins. As the concentration of free lamin chains increases, the second term in Eq. 5 becomes non-negligible, altering the off-rates in a concentration-dependent manner (Fig. 5E). At these concentrations, such as when $c = 3.3c^*$, the off-rates increase monotonically and mostly depend on head-tail association affinity, visually independent of the lamin-shell attraction strength in our simulations (Fig. 5F) (see Supplementary Material Fig. S23). These results imply that increasing lamin head-tail association strength can cause the dissociation of lamin chains from their aggregates at the periphery, often accompanied by a thicker (nematic) layer of lamin chains at the periphery. This is compatible with experimental observations of suppressed (mutant) lamin dissociation from HGPS lamina [7].

IV. DISCUSSION

The nuclear lamina can adapt to changing physiochemical and mechanical conditions by altering the concentration and solvation properties of its main constituents, lamin proteins. In this study, we model supramolecular structures of lamin proteins as stiff, short polymer chains. This over-simplification allows us to explore the physical principles and relative interactions that can lead to experimentally observed morphological and kinetic changes in lamin (particularly A-type lamins) phase behaviour associated with laminopathies such as accelerated aging (i.e., progeria). In our simulations, the spherical and rigid confinement represents the nuclear void bounded by the nuclear membrane (INM), which can interact with nuclear lamins. The lamin model attempts to mimic the complex head-tail association of lamin fibers by incorporating asymmetric interactions between chain ends. This simple model reproduces the nematic phase formation, nuclear lamina thickening, and suppressed dissociation kinetics of mutant lamin proteins observed in diseased cell nuclei [7, 8, 39, 43]. It also emulates certain properties of the nuclear lamina in healthy cells, all by exploiting lamin-INM interactions, lamin-lamin association affinities, and lamin concentration. Below, we will further discuss the potential implications of our calculations in the context of structural biology of cell nuclei in health and disease.

A. Alterations in lamin localization to the nuclear periphery can lead to structural anomalies in nuclear lamina

Once cell division initiates, the nuclear lamina disassembles via a hyperphosphorylation mechanism and later re-assembles around the replicated chromosomes of the sister cells [11, 12]. A prerequisite for the re-asssembly of the nuclear lamina is the localization of some, if not all, lamin proteins (mostly lamin A/C since lamin B is often attached to INM) or their supramolecular structures to the nuclear periphery. In this way, lamins can associate with one another and/or with the INM to form a quasi-2d meshwork underneath the INM. Importantly, this self-assembled and dynamic meshwork must provide mechanical support to the nucleus while ensuring nuclear shape stability in a healthy cell.

In our simulations, the localization of rod-like lamin chains results from the competition between the lamin self-affinity and their tendency to bind to the periphery of the spherical shell (i.e., the INM) (Fig. 4). A lamin-shell affinity comparable to the lamin-lamin (head-to-tail) association strength ensures the formation of a uniformly distributed lamin layer at the periphery, where lamins organize in a more random fashion, consistent with the lamin organization in healthy cells (Fig. 4G).

The nuclear lamina becomes thicker and mechanically more rigid in HGPS due to the excess aggregation of mutant lamin A, progerin, at the nuclear lamina [7, 41, 42], causing decreasing morphological adaptability in the disease. From a molecular perspective, progerin remains farnesylated after post-translational modifications. Farnesylation promotes progerin's membrane association and enhances its thermodynamic stability compared to *wt*-lamin A [68, 69]. Notably, increased hydrophobic interactions have also been reported between the tail domain of progerin and INM proteins, such as SUN1 and Emerin [28]. These experiments collectively suggest that truncated lamin A, progerin, might have a stronger tendency to associate with the INM compared to *wt*-lamin A. Our simulations support this, showing that strong lamin-shell attraction (i.e., strong binding to the INM) can lead to strong aggregation of chains towards the periphery (Fig. 2, 3). Further, under a finite lamin-lamin association strength, the strong peripheral localization gives rise to nematic-phase domains in simulations, which were realized experimentally both *in vitro* [36, 70] and *in vivo* [7]. Noteworthy, long semi-flexible chains were shown to form global nematic phases (see Supplementary Material Fig. S4) [48–51], unlike the finite-size domains observed in our study, further supporting a view that in progeria, lamin fibers could be shorter than their healthy counterparts.

Moreover, the formation of nematic domains may require stronger hydrophobic interactions between lamins at the lamina surface, which is often the case in liquid crystals [47, 71–74]. Studies on the crystal structure of progeria mutant $S143F$ suggested the formation of

X-shaped disulfide bonds in the central rod domains of progerin [18]. This implies that hydrophobic interactions can play a role in altering the morphology of the lamina meshwork [18, 69], possibly bringing cysteine residues of progerin molecules close to one another. In light of our results, which treat the lamin proteins as hydrophobic (except their head and tail domains), the enhanced hydrophobic interactions in HGPS could also contribute to the formation of nematic phase domains at the nuclear lamina.

B. Inter-lamin affinity can dictate nuclear lamina thickening

In addition to the formation of nematic domains, nuclear lamina thickening also serves as a key disease hallmark along with abnormal nuclear shape [6, 8, 24–29, 64]. Accordingly, as progerin concentration increases parallel to the disease progression, the nuclear lamina thickens as toxic mutant proteins accumulate at the periphery [8, 43]. Such aggregation can be promoted by an increase in the effective affinity of mutant lamins towards each other or the INM. This view is also consistent with the observed decrease in exchange rates of progerin [7], indicating an increase in the interaction energies between mutant proteins and their molecular environment. In line with this, our simulations suggest that in HGPS, the thickening of the nuclear lamina near the periphery can be the result of an interplay between lamin localization and increasing lamin-lamin association (e.g., head-tail) as the nuclear concentration of mutant lamins increases (Fig. 4). In fact, relatively higher head-tail association strength readily results in thicker lamin layer and chain aggregation in our simulations, suggesting a dominant effect for inter-lamin interactions.

Consistent with this view, permanent farnesylation of progerin enhances its binding properties to the INM compared to *wt*-lamin A [69], as discussed earlier. However, the farnesyl group remains sequestered within a hydrophobic region in the tail domain unless physiological concentrations of divalent ions, such as Ca^{2+}, are present at the nuclear periphery [64]. Without calcium ions, the farnesyl group only acts as a reversible crosslink, temporarily associating with membrane proteins, but can still dissociate into the nucleoplasm, a characteristic of healthy nuclei [19, 69]. Calcium can induce a conformational change in progerin, opening up the tail domain's Ig-like fold, and exposing the farnesyl group for molecular interactions. This exposure can facilitate the formation of stronger intermolecular interactions with both other lamin molecules (e.g., progerin and other unaltered lamins) and the INM [26, 64]. These experimental observations are consistent with our MD simulations, where nuclear lamins become constrained to the INM when both head-tail association and lamin-shell association strengths are high (i.e., $U_{\mathrm{HT}} \geq U_{\mathrm{LN}}$) (Fig. 4), suggesting an intricate interplay of intermolecular interactions promoting lamina thickening at the periphery.

C. Dissociation kinetics of lamins from nuclear lamina can have a concentration dependence

Photobleaching experiments suggest that peripherally bound lamins could exchange with their nucleoplasmic counterparts in healthy cells [7]. One possible mechanism by which free lamin A might influence the kinetics of lamin exchange between the nuclear lamina structure and nucleoplasmic (free) lamin in health could be facilitated dissociation (FD). FD is a concentration-dependent dissociation mechanism, originally discovered in the context of protein-DNA interactions [61, 65, 66, 75]. FD causes an increased exchange (dissociation) rate for a ligand attached to its binding site when free ligands are present in the solution. The mechanism is based on the molecular-scale competition between the two ligands at the binding site (such as a third lamin) (see Supplementary Material Fig. S11). Nucleoplasmic lamin proteins can likely compete with their bound counterparts in the nuclear lamina, leading to rapidly decaying signals observed in the experiments. Our simulations demonstrate such a concentration-dependent mechanism for lamin chains (Fig. 5). In contrast, the exchange rate drops in HGPS [7], possibly due to increasing intermolecular interactions between the mutant protein and the nuclear lamina and depletion of lamin from nucleoplasm. Consistently, our calculations show that increased lamin-lamin affinity reduces dissociation rates while promoting further lamin accommodation near the periphery and eventually affecting the thickness of the lamin layer (Fig. 4, 5). Furthermore, unlike HGPS cells, the accumulation of lamin proteins (specifically *wt*-lamin A) increases nuclear stability in some healthy cell lines [41, 42], and even correlates with decreased DNA double-strand breaks [42]. Thus, based on the available literature and our simulations, we speculate that lamin unbinding kinetics from the nuclear lamina could also have structural consequences, leading to either a highly adaptive, mechanically soft lamina or a highly stable but mechanically brittle one.

In summary, we employed a coarse-grained polymer model of lamin supramolecular structures to investigate the key physical interactions that can drive the abnormal self-assembly of lamin proteins in the formation of the nuclear lamina, with a particular focus on HGPS (progeria syndrome). Our findings suggest that enhanced intermolecular interactions among mutant lamins can lead to specific disease hallmarks in the nuclear lamina structure. The simulations reveal an interplay between lamin-lamin and lamin-INM interactions in a concentration-dependent manner, demonstrating how this interplay can reduce lamin exchange rates, cause lamina thickening, and promote the formation of nematic microdomains, as observed in HGPS. Given the highly distorted nuclear morphology

and mechanics in HGPS [8, 29, 38–40], future studies could benefit from more sophisticated models to better understand these changes. For instance, replacing spherical confinement with elastic shell models [76, 77] filled with chromatin [78] could provide deeper insights into nuclear shape alterations associated with the disease.

V. ACKNOWLEDGMENTS

AE acknowledges E.J. Banigan for his suggestions on disseminating this work. This research was supported by the National Science Center, EU's H2020 Programme, and MSCA Grant Agreement No. 945339 Poland [Grant Polonez Bis No. 2021/43/P/ST3/01833], as well as TUBITAK, The Scientific and Technological Research Council of Turkey [1001 Grant No. 122F309].

[1] Ueli Aebi, Julie Cohn, Loren Buhle, and Larry Gerace. The nuclear lamina is a meshwork of intermediate-type filaments. *Nature*, 323(6088):560–564, Oct 1986. doi: 10.1038/323560a0.

[2] Nico Stuurman, Susanne Heins, and Ueli Aebi. Nuclear lamins: Their structure, assembly, and interactions. *Journal of Structural Biology*, 122(1–2):42–66, 1998. doi: 10.1006/jsbi.1998.3987.

[3] Yosef Gruenbaum, Katherine L. Wilson, Amnon Harel, Michal Goldberg, and Merav Cohen. Review: Nuclear lamins—structural proteins with fundamental functions. *Journal of Structural Biology*, 129(2–3):313–323, Apr 2000. doi:10.1006/jsbi.2000.4216.

[4] Yosef Gruenbaum, Robert D Goldman, Ronit Meyuhas, Erez Mills, Ayelet Margalit, Alexandra Fridkin, Yaron Dayani, Miron Prokocimer, and Avital Enosh. The nuclear lamina and its functions in the nucleus. *International Review of Cytology*, page 1–62, 2003. doi: 10.1016/s0074-7696(03)01001-5.

[5] Amir Vahabikashi, Stephen A. Adam, Ohad Medalia, and Robert D. Goldman. Nuclear lamins: Structure and function in mechanobiology. *APL Bioengineering*, 6(1), Feb 2022. doi:10.1063/5.0082656.

[6] Veronika Butin-Israeli, Stephen A. Adam, Anne E. Goldman, and Robert D. Goldman. Nuclear lamin functions and disease. *Trends in Genetics*, 28(9):464–471, Sep 2012. doi:10.1016/j.tig.2012.06.001.

[7] Kris Noel Dahl, Paola Scaffidi, Mohammad F. Islam, Arjun G. Yodh, Katherine L. Wilson, and Tom Misteli. Distinct structural and mechanical properties of the nuclear lamina in Hutchinson–Gilford progeria syndrome. *Proceedings of the National Academy of Sciences*, 103(27): 10271–10276, Jul 2006. doi:10.1073/pnas.0601058103.

[8] Robert D. Goldman, Dale K. Shumaker, Michael R. Erdos, Maria Eriksson, Anne E. Goldman, Leslie B. Gordon, Yosef Gruenbaum, Satya Khuon, Melissa Mendez, Renée Varga, and et al. Accumulation of mutant lamin A causes progressive changes in nuclear architecture in hutchinson–gilford progeria syndrome. *Proceedings of the National Academy of Sciences*, 101(24):8963–8968, Jun 2004. doi:10.1073/pnas.0402943101.

[9] Chloe M. Funkhouser, Rastko Sknepnek, Takeshi Shimi, Anne E. Goldman, Robert D. Goldman, and Monica Olvera de la Cruz. Mechanical model of blebbing in nuclear lamin meshworks. *Proceedings of the National Academy of Sciences*, 110(9):3248–3253, Feb 2013. doi: 10.1073/pnas.1300215110.

[10] Larry Gerace and Brian Burke. Functional organization of the nuclear envelope. *Annual Review of Cell Biology*, 4(1):335–374, Nov 1988. doi: 10.1146/annurev.cb.04.110188.002003.

[11] E.A. Nigg. Assembly and cell cycle dynamics of the nuclear lamina. *Seminars in Cell Biology*, 3(4):245–253, Aug 1992. doi:10.1016/1043-4682(92)90026-r.

[12] Stephan Güttinger, Eva Laurell, and Ulrike Kutay. Orchestrating nuclear envelope disassembly and reassembly during mitosis. *Nature Reviews Molecular Cell Biology*, 10(3):178–191, Mar 2009. doi:10.1038/nrm2641.

[13] D Z Fisher, N Chaudhary, and G Blobel. DNA sequencing of nuclear lamins A and C reveals primary and secondary structural homology to intermediate filament proteins. *Proceedings of the National Academy of Sciences*, 83(17):6450–6454, Sep 1986. doi: 10.1073/pnas.83.17.6450.

[14] Robert D. Moir, Anne D. Donaldson, and Murray Stewart. Expression in escherichia coli of human lamins A and C: influence of head and tail domains on assembly properties and paracrystal formation. *Journal of Cell Science*, 99(2):363–372, Jun 1991. doi:10.1242/jcs.99.2.363.

[15] E. Heitlinger, M. Peter, A. Lustig, W. Villiger, E.A. Nigg, and U. Aebi. The role of the head and tail domain in lamin structure and assembly: Analysis of bacterially expressed chicken Lamin A and truncated B2 lamins. *Journal of Structural Biology*, 108(1):74–91, Jan 1992. doi:10.1016/1047-8477(92)90009-y.

[16] R D Moir, M Montag-Lowy, and R D Goldman. Dynamic properties of nuclear lamins: lamin B is associated with sites of dna replication. *The Journal of cell biology*, 125 (6):1201–1212, Jun 1994. doi:10.1083/jcb.125.6.1201.

[17] Yagmur Turgay, Matthias Eibauer, Anne E. Goldman, Takeshi Shimi, Maayan Khayat, Kfir Ben-Harush, Anna Dubrovsky-Gaupp, K. Tanuj Sapra, Robert D. Goldman, and Ohad Medalia. The molecular architecture of lamins in somatic cells. *Nature*, 543(7644):261–264, Mar 2017. doi:10.1038/nature21382.

[18] Jinsook Ahn, Soyeon Jeong, So-mi Kang, Inseong Jo, Bum-Joon Park, and Nam-Chul Ha. Crystal structure of progeria mutant S143F lamin A/C reveals increased hydrophobicity driving nuclear deformation. *Communications Biology*, 5(1), Mar 2022. doi:10.1038/s42003-022-03212-3.

[19] A E Goldman, R D Moir, M Montag-Lowy, M Stewart, and R D Goldman. Pathway of incorporation of microinjected lamin A into the nuclear envelope. *The Journal of cell biology*, 119(4):725–735, Nov 1992. doi: 10.1083/jcb.119.4.725.

[20] Robert D. Goldman, Yosef Gruenbaum, Robert D. Moir, Dale K. Shumaker, and Timothy P. Spann. Nu-

clear lamins: Building blocks of nuclear architecture. *Genes & Development*, 16(5):533–547, Mar 2002. doi: 10.1101/gad.960502.

[21] K. Tanuj Sapra, Zhao Qin, Anna Dubrovsky-Gaupp, Ueli Aebi, Daniel J. Müller, Markus J. Buehler, and Ohad Medalia. Nonlinear mechanics of lamin filaments and the meshwork topology build an emergent nuclear lamina. *Nature Communications*, 11(1), Dec 2020. doi: 10.1038/s41467-020-20049-8.

[22] Takeshi Shimi, Mark Kittisopikul, Joseph Tran, Anne E. Goldman, Stephen A. Adam, Yixian Zheng, Khuloud Jaqaman, and Robert D. Goldman. Structural organization of nuclear lamins A, C, B1, and B2 revealed by superresolution microscopy. *Molecular Biology of the Cell*, 26(22):4075–4086, Nov 2015. doi:10.1091/mbc.e15-07-0461.

[23] Bruce Nmezi, Jianquan Xu, Rao Fu, Travis J. Armiger, Guillermo Rodriguez-Bey, Juliana S. Powell, Hongqiang Ma, Mara Sullivan, Yiping Tu, Natalie Y. Chen, and et al. Concentric organization of A- and B-type lamins predicts their distinct roles in the spatial organization and stability of the nuclear lamina. *Proceedings of the National Academy of Sciences*, 116(10):4307–4315, Feb 2019. doi:10.1073/pnas.1810070116.

[24] Jinsook Ahn, Jinwook Lee, Soyeon Jeong, Inseong Jo, So-mi Kang, Bum-Joon Park, and Nam-Chul Ha. Structural basis for the interaction between unfarnesylated progerin and the Ig-like domain of lamin A/C in premature aging disorders. *Biochemical and Biophysical Research Communications*, 637:210–217, Dec 2022. doi: 10.1016/j.bbrc.2022.10.070.

[25] Maria Chiara Lionetti, Silvia Bonfanti, Maria Rita Fumagalli, Francesc Font-Clos, Giulio Costantini, Oleksandr Chepizhko, Stefano Zapperi, and Caterina La Porta. Chromatin and cytoskeletal tethering determine nuclear morphology in progerin expressing cells. *Biophysical Journal*, 120(3), Feb 2021. doi: 10.1016/j.bpj.2020.11.1768.

[26] Agnieszka Kalinowski, Peter N. Yaron, Zhao Qin, Siddharth Shenoy, Markus J. Buehler, Mathias Lösche, and Kris Noel Dahl. Interfacial binding and aggregation of lamin a tail domains associated with Hutchinson–Gilford Progeria syndrome. *Biophysical Chemistry*, 195:43–48, Dec 2014. doi:10.1016/j.bpc.2014.08.005.

[27] Jungwon Hah and Dong-Hwee Kim. Deciphering nuclear mechanobiology in laminopathy. *Cells*, 8(3):231, Mar 2019. doi:10.3390/cells8030231.

[28] Noelle J. Batista, Sanket G. Desai, Alexis M. Perez, Alexa Finkelstein, Rachel Radigan, Manrose Singh, Aaron Landman, Brian Drittel, Daniella Abramov, Mina Ahsan, and et al. The Molecular and Cellular basis of Hutchinson-Gilford Progeria Syndrome and Potential Treatments. *Genes*, 14(3):602, Feb 2023. doi: 10.3390/genes14030602.

[29] Paola Scaffidi and Tom Misteli. Reversal of the cellular phenotype in the premature aging disease Hutchinson-Gilford Progeria syndrome. *Nature Medicine*, 11(4): 440–445, Mar 2005. doi:10.1038/nm1204.

[30] Maria Eriksson, W. Ted Brown, Leslie B. Gordon, Michael W. Glynn, Joel Singer, Laura Scott, Michael R. Erdos, Christiane M. Robbins, Tracy Y. Moses, Peter Berglund, and et al. Recurrent de novo point mutations in lamin A cause Hutchinson–Gilford progeria syndrome. *Nature*, 423(6937):293–298, Apr 2003. doi: 10.1038/nature01629.

[31] Jan Lammerding, Loren G. Fong, Julie Y. Ji, Karen Reue, Colin L. Stewart, Stephen G. Young, and Richard T. Lee. Lamins A and C but not lamin B1 regulate nuclear mechanics. *Journal of Biological Chemistry*, 281(35):25768–25780, Sep 2006. doi: 10.1074/jbc.m513511200.

[32] F. Lin and H.J. Worman. Structural organization of the human gene encoding nuclear lamin A and nuclear lamin C. *Journal of Biological Chemistry*, 268(22):16321–16326, Aug 1993. doi:10.1016/s0021-9258(19)85424-8.

[33] Hartwig Hennekes and Erich A. Nigg. The role of isoprenylation in membrane attachment of nuclear lamins. a single point mutation prevents proteolytic cleavage of the lamin A precursor and confers membrane binding properties. *Journal of Cell Science*, 107(4):1019–1029, Apr 1994. doi:10.1242/jcs.107.4.1019.

[34] Jinsook Ahn, Inseong Jo, So-mi Kang, Seokho Hong, Suhyeon Kim, Soyeon Jeong, Yong-Hak Kim, Bum-Joon Park, and Nam-Chul Ha. Structural basis for lamin assembly at the molecular level. *Nature Communications*, 10(1), Aug 2019. doi:10.1038/s41467-019-11684-x.

[35] Mingyue Zheng, Guoxiang Jin, and Zhongjun Zhou. Post-translational modification of lamins: Mechanisms and functions. *Frontiers in Cell and Developmental Biology*, 10, May 2022. doi:10.3389/fcell.2022.864191.

[36] Pekka Taimen, Katrin Pfleghaar, Takeshi Shimi, Dorothee Möller, Kfir Ben-Harush, Michael R. Erdos, Stephen A. Adam, Harald Herrmann, Ohad Medalia, Francis S. Collins, and et al. A progeria mutation reveals functions for lamin A in nuclear assembly, architecture, and chromosome organization. *Proceedings of the National Academy of Sciences*, 106(49):20788–20793, Dec 2009. doi:10.1073/pnas.0911895106.

[37] Andrew D. Stephens, Patrick Z. Liu, Edward J. Banigan, Luay M. Almassalha, Vadim Backman, Stephen A. Adam, Robert D. Goldman, and John F. Marko. Chromatin histone modifications and rigidity affect nuclear morphology independent of lamins. *Molecular Biology of the Cell*, 29(2):220–233, Jan 2018. doi:10.1091/mbc.e17-06-0410.

[38] Annachiara De Sandre-Giovannoli, Rafaelle Bernard, Pierre Cau, Claire Navarro, Jeanne Amiel, Irene Boccaccio, Stanislas Lyonnet, Colin L. Stewart, Arnold Munnich, Martine Le Merrer, and et al. Lamin A truncation in Hutchinson-Gilford Progeria. *Science*, 300(5628): 2055–2055, Jun 2003. doi:10.1126/science.1084125.

[39] Paola Scaffidi and Tom Misteli. Lamin A-dependent nuclear defects in human aging. *Science*, 312(5776): 1059–1063, May 2006. doi:10.1126/science.1127168.

[40] Paola Scaffidi and Tom Misteli. Lamin A-dependent misregulation of adult stem cells associated with accelerated ageing. *Nature Cell Biology*, 10(4):452–459, Mar 2008. doi:10.1038/ncb1708.

[41] Jae-Won Shin, Kyle R. Spinler, Joe Swift, Joel A. Chasis, Narla Mohandas, and Dennis E. Discher. Lamins regulate cell trafficking and lineage maturation of adult human hematopoietic cells. *Proceedings of the National Academy of Sciences*, 110(47):18892–18897, Nov 2013. doi:10.1073/pnas.1304996110.

[42] Joe Swift, Irena L. Ivanovska, Amnon Buxboim, Takamasa Harada, P. C. Dingal, Joel Pinter, J. David Pajerowski, Kyle R. Spinler, Jae-Won Shin, Manorama

Tewari, and et al. Nuclear lamin-A scales with tissue stiffness and enhances matrix-directed differentiation. *Science*, 341(6149), Aug 2013. doi:10.1126/science.1240104.

[43] Yuxuan Guo, Youngjo Kim, Takeshi Shimi, Robert D. Goldman, and Yixian Zheng. Concentration-dependent lamin assembly and its roles in the localization of other nuclear proteins. *Molecular Biology of the Cell*, 25(8): 1287–1297, Apr 2014. doi:10.1091/mbc.e13-11-0644.

[44] Kris Noel Dahl, Samuel M. Kahn, Katherine L. Wilson, and Dennis E. Discher. The nuclear envelope lamina network has elasticity and a compressibility limit suggestive of a molecular shock absorber. *Journal of Cell Science*, 117(20):4779–4786, Sep 2004. doi:10.1242/jcs.01357.

[45] Theo Odijk. Theory of lyotropic polymer liquid crystals. *Macromolecules*, 19(9):2313–2329, Sep 1986. doi: 10.1021/ma00163a001.

[46] Alexandre Blumstein. *Liquid crystalline order in polymers*. Academic Press, 1978.

[47] Aykut Erbas and Monica Olvera de la Cruz. Morphology-enhanced conductivity in dry ionic liquids. *Physical Chemistry Chemical Physics*, 18(9):6441–6450, 2016. doi: 10.1039/c5cp07090b.

[48] Arash Nikoubashman, Daniel A. Vega, Kurt Binder, and Andrey Milchev. Semiflexible polymers in spherical confinement: Bipolar orientational order versus tennis ball states. *Physical Review Letters*, 118(21), May 2017. doi: 10.1103/physrevlett.118.217803.

[49] Andrey Milchev, Sergei A. Egorov, Arash Nikoubashman, and Kurt Binder. Adsorption and structure formation of semiflexible polymers on spherical surfaces. *Polymer*, 145:463–472, Jun 2018. doi: 10.1016/j.polymer.2018.04.054.

[50] Andrey Milchev, Sergei A. Egorov, Arash Nikoubashman, and Kurt Binder. Conformations and orientational ordering of semiflexible polymers in spherical confinement. *The Journal of Chemical Physics*, 146(19), May 2017. doi:10.1063/1.4983131.

[51] Andrey Milchev, Sergei A. Egorov, Daniel A. Vega, Kurt Binder, and Arash Nikoubashman. Densely packed semiflexible macromolecules in a rigid spherical capsule. *Macromolecules*, 51(5):2002–2016, Feb 2018. doi: 10.1021/acs.macromol.7b02643.

[52] Robert D. Moir, Miri Yoon, Satya Khuon, and Robert D. Goldman. Nuclear lamins A and B1: different pathways of assembly during nuclear envelope formation in living cells. *The Journal of Cell Biology*, 151(6):1155–1168, Dec 2000. doi:10.1083/jcb.151.6.1155.

[53] Takeshi Shimi, Katrin Pfleghaar, Shin-ichiro Kojima, Chan-Gi Pack, Irina Solovei, Anne E. Goldman, Stephen A. Adam, Dale K. Shumaker, Masataka Kinjo, Thomas Cremer, and et al. The A- and B-type nuclear lamin networks: Microdomains involved in chromatin organization and transcription. *Genes & Development*, 22 (24):3409–3421, Dec 2008. doi:10.1101/gad.1735208.

[54] Kurt Kremer and Gary S. Grest. Dynamics of entangled linear polymer melts: a molecular-dynamics simulation. *The Journal of Chemical Physics*, 92(8):5057–5086, Apr 1990. doi:10.1063/1.458541.

[55] Monika Zwerger, Heidi Roschitzki-Voser, Reto Zbinden, Celine Denais, Harald Herrmann, Jan Lammerding, Markus G. Grütter, and Ohad Medalia. Altering lamina assembly identifies lamina-dependent and -independent functions for A-type lamins. *Journal of Cell Science*, Jan 2015. doi:10.1242/jcs.171843.

[56] E Heitlinger, M Peter, M Häner, A Lustig, U Aebi, and E A Nigg. Expression of chicken lamin B2 in escherichia coli: Characterization of its structure, assembly, and molecular interactions. *The Journal of cell biology*, 113 (3):485–495, May 1991. doi:10.1083/jcb.113.3.485.

[57] Aidan P. Thompson, H. Metin Aktulga, Richard Berger, Dan S. Bolintineanu, W. Michael Brown, Paul S. Crozier, Pieter J. in 't Veld, Axel Kohlmeyer, Stan G. Moore, Trung Dac Nguyen, and et al. LAMMPS - a flexible simulation tool for particle-based materials modeling at the atomic, meso, and continuum scales. *Computer Physics Communications*, 271:108171, Feb 2022. doi:10.1016/j.cpc.2021.108171.

[58] Charles R. Harris, K. Jarrod Millman, Stéfan J. van der Walt, Ralf Gommers, Pauli Virtanen, David Cournapeau, Eric Wieser, Julian Taylor, Sebastian Berg, Nathaniel J. Smith, and et al. Array programming with NumPy. *Nature*, 585(7825):357–362, Sep 2020. doi: 10.1038/s41586-020-2649-2.

[59] William Humphrey, Andrew Dalke, and Klaus Schulten. VMD: Visual molecular dynamics. *Journal of Molecular Graphics*, 14(1):33–38, Feb 1996. doi:10.1016/0263-7855(96)00018-5.

[60] Alexander Stukowski. Visualization and analysis of atomistic simulation data with OVITO–The Open Visualization Tool. *Modelling and Simulation in Materials Science and Engineering*, 18(1):015012, Dec 2009. doi: 10.1088/0965-0393/18/1/015012.

[61] Zafer Kosar, A. Göktuĝ Attar, and Aykut Erbas. Facilitated dissociation of nucleoid-associated proteins from DNA in the bacterial confinement. *Biophysical Journal*, 121(7):1119–1133, Apr 2022. doi: 10.1016/j.bpj.2022.03.002.

[62] Aykut Erbas and John F Marko. How do DNA-bound proteins leave their binding sites? the role of facilitated dissociation. *Current Opinion in Chemical Biology*, 53: 118–124, Dec 2019. doi:10.1016/j.cbpa.2019.08.007.

[63] Mihir R. Khadilkar and Arash Nikoubashman. Self-assembly of semiflexible polymers confined to thin spherical shells. *Soft Matter*, 14(33):6903–6911, 2018. ISSN 1744-683X. doi:10.1039/c8sm01170b.

[64] Agnieszka Kalinowski, Zhao Qin, Kelli Coffey, Ravi Kodali, Markus J. Buehler, Mathias Lösche, and Kris Noel Dahl. Calcium causes a conformational change in lamin a tail domain that promotes farnesyl-mediated membrane association. *Biophysical Journal*, 104(10):2246–2253, May 2013. doi:10.1016/j.bpj.2013.04.016.

[65] Chandra P. Joshi, Debashis Panda, Danya J. Martell, Nesha May Andoy, Tai-Yen Chen, Ahmed Gaballa, John D. Helmann, and Peng Chen. Direct substitution and assisted dissociation pathways for turning off transcription by a MerR-family metalloregulator. *Proceedings of the National Academy of Sciences*, 109(38):15121–15126, Sep 2012. doi:10.1073/pnas.1208508109.

[66] Ramsey I. Kamar, Edward J. Banigan, Aykut Erbas, Rebecca D. Giuntoli, Monica Olvera de la Cruz, Reid C. Johnson, and John F. Marko. Facilitated dissociation of transcription factors from single DNA binding sites. *Proceedings of the National Academy of Sciences*, 114(16), Mar 2017. doi:10.1073/pnas.1701884114.

[67] Charles E. Sing, Monica Olvera de la Cruz, and John F. Marko. Multiple-binding-site mechanism explains concentration-dependent unbinding rates of DNA-binding proteins. *Nucleic Acids Research*, 42(6):

3783–3791, Jan 2014. doi:10.1093/nar/gkt1327.

[68] Zhao Qin, Agnieszka Kalinowski, Kris Noel Dahl, and Markus J. Buehler. Structure and stability of the lamin a tail domain and HGPS mutant. *Journal of Structural Biology*, 175(3):425–433, Sep 2011. doi: 10.1016/j.jsb.2011.05.015.

[69] Zhao Qin and Markus J. Buehler. Computational and theoretical modeling of intermediate filament networks: Structure, mechanics and disease. *Acta Mechanica Sinica*, 28(4):941–950, Aug 2012. doi:10.1007/s10409-012-0124-5.

[70] T. Dechat, S. A. Adam, P. Taimen, T. Shimi, and R. D. Goldman. Nuclear lamins. *Cold Spring Harbor Perspectives in Biology*, 2(11), Sep 2010. doi: 10.1101/cshperspect.a000547.

[71] Takahiro Ichikawa, Masafumi Yoshio, Atsushi Hamasaki, Tomohiro Mukai, Hiroyuki Ohno, and Takashi Kato. Self-organization of room-temperature ionic liquids exhibiting liquid-crystalline bicontinuous cubic phases: formation of nano-ion channel networks. *Journal of the American Chemical Society*, 129(35):10662–10663, Aug 2007. doi: 10.1021/ja0740418.

[72] Takahiro Ichikawa, Masafumi Yoshio, Atsushi Hamasaki, Junko Kagimoto, Hiroyuki Ohno, and Takashi Kato. 3D interconnected ionic nano-channels formed in polymer films: Self-organization and polymerization of thermotropic bicontinuous cubic liquid crystals. *Journal of the American Chemical Society*, 133(7):2163–2169, Jan 2011. doi:10.1021/ja106707z.

[73] Masafumi Yoshio, Takayoshi Kagata, Koji Hoshino, Tomohiro Mukai, Hiroyuki Ohno, and Takashi Kato. One-dimensional ion-conductive polymer films: alignment and fixation of ionic channels formed by self-organization of polymerizable columnar liquid crystals. *Journal of the American Chemical Society*, 128(16):5570–5577, Mar 2006. doi:10.1021/ja0606935.

[74] Alessandro Triolo, Olga Russina, Hans-Jurgen Bleif, and Emanuela Di Cola. Nanoscale segregation in room temperature ionic liquids. *The Journal of Physical Chemistry B*, 111(18):4641–4644, Feb 2007. doi:10.1021/jp067705t.

[75] Katelyn Dahlke, Jing Zhao, Charles E. Sing, and Edward J. Banigan. Force-dependent facilitated dissociation can generate Protein-DNA catch bonds. *Biophysical Journal*, 117(6):1085–1100, Sep 2019. doi: 10.1016/j.bpj.2019.07.044.

[76] Ashesh Ghosh and Andrew J. Spakowitz. Local changes in protein filament properties drive large-scale membrane transformations involved in endosome tethering and fusion. *Soft Matter*, 20(32):6332–6342, 2024. doi: 10.1039/d4sm00299g.

[77] You-Lu Liu, You-Liang Zhu, Yan-Chun Li, and Zhong-Yuan Lu. Exploring the interplay of liquid crystal orientation and spherical elastic shell deformation in spatial confinement. *Physical Chemistry Chemical Physics*, 26(7):6180–6188, 2024. ISSN 1463-9076. doi: 10.1039/d3cp04479c.

[78] Ali Goktug Attar, Jaroslaw Paturej, Edward J. Banigan, and Aykut Erbas. Chromatin phase separation and nuclear shape fluctuations are correlated in a polymer model of the nucleus. *Nucleus*, 15(1), May 2024. doi: 10.1080/19491034.2024.2351957.

[79] Martin Girard, Monica Olvera de la Cruz, John F. Marko, and Aykut Erbas. Heterogeneous flexibility can contribute to chromatin segregation in the cell nucleus. *Physical Review E*, 110(1), Jul 2024. doi: 10.1103/physreve.110.014403.

[80] J. S. Graham, R. C. Johnson, and J. F. Marko. Concentration-dependent exchange accelerates turnover of proteins bound to double-stranded DNA. *Nucleic Acids Research*, 39(6):2249–2259, Nov 2010. doi: 10.1093/nar/gkq1140.

[81] Harald Herrmann, Harald Bär, Laurent Kreplak, Sergei V. Strelkov, and Ueli Aebi. Intermediate filaments: from cell architecture to nanomechanics. *Nature Reviews Molecular Cell Biology*, 8(7):562–573, Jul 2007. doi:10.1038/nrm2197.

[82] Markus Klapper, Kay Exner, Anja Kempf, Claudia Gehrig, Nico Stuurman, Paul A. Fisher, and Georg Krohne. Assembly of A- and B-type lamins studied in vivo with the baculovirus system. *Journal of Cell Science*, 110(20):2519–2532, Oct 1997. doi: 10.1242/jcs.110.20.2519.

[83] M. Peter, G.T. Kitten, C.F. Lehner, K. Vorburger, S.M. Bailer, G. Maridor, and E.A. Nigg. Cloning and sequencing of cdna clones encoding chicken lamins A and B1 and comparison of the primary structures of vertebrate a- and B-type lamins. *Journal of Molecular Biology*, 208 (3):393–404, Aug 1989. doi:10.1016/0022-2836(89)90504-4.

[84] Michael Rubinstein and Ralph H. Colby. *Polymer Physics*. Oxford University press, 2016.